



ON THE AEROELASTIC BEHAVIOUR OF RECTANGULAR CYLINDERS IN CROSS-FLOW

P. HÉMON[†]

Institut Aérotechnique/CNAM, 15 rue Marat, F-78210 Saint-Cyr l'Ecole, France

AND

F. SANTI

*CNAM, Department of Mathematics, 192 rue Saint-Martin, F-75141 Paris
Cedex 03, France*

(Received 31 May 2001, and in final form 21 February 2002)

An experimental and numerical study of the aeroelastic behaviour of elongated rectangular and square cylinders is presented. The main results are for a rectangular section with an aspect ratio of 2. The experiments were performed with a flexible cylinder clamped at both ends. This configuration leads to unusual lock-in of the vortex shedding with different bending modes, although the final steady oscillations occur in the fundamental mode. The galloping regime is also investigated, and the effect of free-stream turbulence intensity. Critical velocities are detected which do not correspond to calculations using the quasi-steady theory. A simple modelling of galloping is proposed to better fit the experiments, but it is shown that some of the configurations, in turbulent flow, are probably interacting with the vortex shedding and make the modelling inefficient. Numerical simulations on a 2-D rectangular section are presented and the resulting wall pressure distributions are analysed using the proper orthogonal decomposition technique. Indicators are proposed in order to link the proper functions with their contribution to the aerodynamic force components, and then a classification of the proper shapes of the decomposition is done. It is shown by comparison between the static case and forced oscillations, in the galloping range, that secondary vortices inside the shear layer become symmetrical and their effect on the forces is cancelled.

© 2002 Elsevier Science Ltd. All rights reserved.

1. INTRODUCTION

1.1. POSITION OF THE STUDY

We consider the oscillations of some elongated cylinders submitted to an air cross-flow. The tested sections of the cylinder are square ($c/e = 1$) and rectangular with an aspect ratio $c/e = 2$, as shown in Fig. 1. In this paper, we will try to describe the aeroelastic behaviour of these sections, mainly the rectangular one. The methods of investigation are 3-D experiments using a long flexible cylinder free to vibrate in a wind tunnel, and 2-D numerical simulations of which the results are analysed using proper orthogonal decompositions. Partial versions of this research work were presented in Hémon & Santi (2000) and Hémon *et al.* (2001). The objective is to obtain a deeper physical understanding of the phenomena in relation to problems of wind-excited structures such as bridge decks and pylons, towers, chimneys, and so on.

[†]Present address: LadHyX, Ecole Polytechnique—CNRS, F-91128 Palaiseau Cedex, France

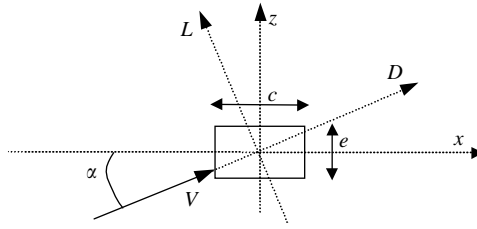


Figure 1. Cross-sectional view, showing source of the geometrical parameters.

Due to the size of the wind tunnel, the flow velocity and the structural characteristics of the model, the Reynolds number of this study, based on the chord length c , is in the range of $5000\text{--}10^4$. This regime is much lower than in the case of practical problems; however, it is reasonably asserted that the physics is qualitatively the same, and only the values of some coefficients are subject to Reynolds number effects. Otherwise, the sharp edges of the bodies studied are generally considered as a justification to the lack of scale effects, although one must be aware that some exceptions can occur.

The paper is organised as follows. Following a review of relevant work, a description of the experimental and numerical tools is given. In particular, a method of analysis by proper orthogonal decomposition is introduced for which new indicators are proposed. The results are presented in Section 3, where an unusual vortex excitation observed during experiments is described. These results are then analysed and discussed in Section 4, where a model of the time-delayed force of galloping is also proposed and compared with experiments.

1.2. OVERVIEW OF THE PROBLEM

Many authors have already written on the behaviour of rectangular sections subjected to cross-flow. Some of the studies are restricted to rigid fixed sections, but the major part is devoted to dynamic problems.

Indeed, the flow can produce transverse vibrations generated by vortex shedding, denoted as vortex-induced vibrations (VIV), and by galloping which is a movement-induced vibration (MIV) type of excitation (Naudascher & Rockwell 1994). The behaviour of the system is modified by the oncoming mean flow velocity V , the angle of attack α and the turbulence characteristics.

It is now well known that alternate vortex shedding produces a strong fluctuating lift force within a narrow frequency band given by the so-called Strouhal number, St . If the structure is flexible enough and has some eigenfrequencies close to that of the shedding, then a resonance effect is possible and large vibrations can occur. In that case, the lock-in phenomenon appears and represents a complex behaviour where the vibration of the beam has a strong influence on the shedding, as in the “chicken and egg” problem.

On the other hand, galloping oscillations were first explained by Den Hartog (1934), who introduced the criterion for the stability of cross-wind oscillations, using the quasi-steady assumption and a linearised approach:

$$C'_z = \left(\frac{\partial C_D}{\partial \alpha} - C_L \right) \sin \alpha + \left(\frac{\partial C_L}{\partial \alpha} + C_D \right) \cos \alpha < 0, \quad (1)$$

where the aerodynamic force coefficients are C_D and C_L with the notations shown in Fig. 1. For small angles of attack, this condition is closely related to the lift slope, a negative value producing a potentially unstable situation, and can be influenced by the

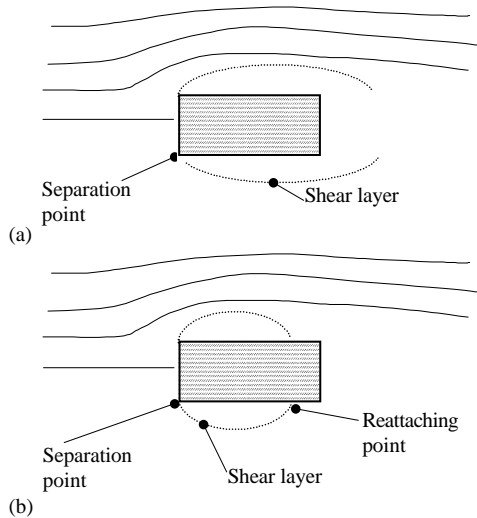


Figure 2. Mean flow around a rectangular section: (a) fully separated; (b) reattached.

upstream flow. Due to the linear approximation, the Den Hartog criterion is able to detect an unstable situation, but it is unable to describe a limit cycle when it occurs. Later, a nonlinear galloping theory was proposed by Novak (Novak 1969, 1972; Novak & Tanaka 1974) for different kinds of section, including the square and short rectangles.

Considering the rectangular cross-sections, it is now admitted that the morphology of the flow around the body is responsible for galloping oscillations (Naudascher & Rockwell 1994; Matsumoto *et al.* 1998). Indeed, the situation of a fully separated flow, as presented in Fig. 2(a), will generate a negative lift slope and the possibility of galloping oscillations. When the flow reattaches on the lateral sides, as in Fig. 2(b), the lift slope becomes generally positive and galloping does not occur. Thus, when the aspect ratio c/e is large enough, the flow always reattaches and these section shapes are stable from the point of view of galloping.

In the case of $c/e=2$, which is the lower possible value of stable sections, upstream turbulence may influence the reattachment as shown by the lift curves in Fig. 3, mainly from Novak (1972). Therefore, this ratio can be considered as critical, because it is able to present all the possible situations: excitation by alternate vortex shedding, galloping, and also stability for these two phenomena, depending on the upstream conditions. Another point is the possibility of coupling between the two phenomena: for example, if the structural conditions are favourable, vortex excitation can trigger galloping oscillations. The usual methods of investigation generally use the flutter derivatives introduced by Scanlan, as in Simiu & Scanlan (1986) for example, which allow the detection of aeroelastic instabilities but do not really explain its mechanism physically. In the case of galloping, the so-called H_1^* coefficient would describe the risk of instability for a given range of reduced velocities, but its explanation should remain in the context of the modelling, and is notably limited to linear behaviour.

1.3. A REVIEW OF PREVIOUS WORK

In the case of a fixed cylinder, Norberg (1993) published some static measurements in smooth flow for small Reynolds numbers, similar to those of this study. Useful results are

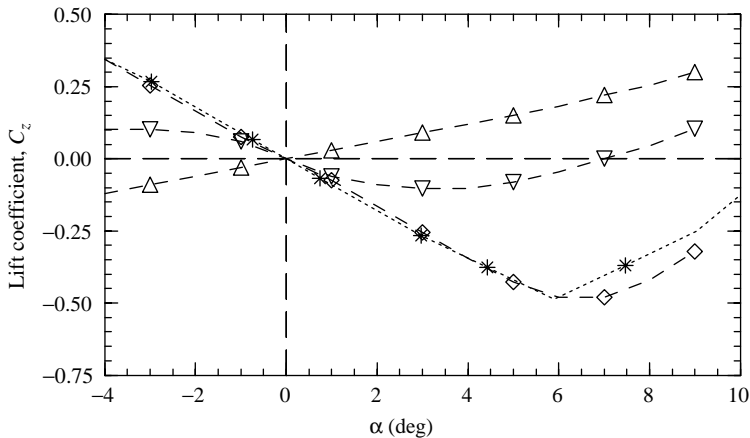


Figure 3. Effect of free-stream turbulence on the lift force coefficient versus angle of attack for the rectangular section from Novak (1972) and Deniz & Staubli (1997): ♦, smooth; ∇, $I=5\%$; △, $I=11\%$; ∗, smooth (Deniz & Staubli 1997).

the Strouhal numbers and the static force coefficients versus the angle of attack for aspect ratios between 1 and 3. Also an interesting numerical approach was given in Davis & More (1982) for cylinders with a cross-sectional shape close to that of a square, but with smaller Reynolds numbers: < 2800 . The effect of the aspect ratio was also studied numerically (Okajima 1988) for low Reynolds numbers, 150–800. One can also find some general results in the review by Naudasher & Rockwell (1994) including the dynamic cases.

In the dynamic range, Nakamura & Nakashima (1986) presented many results on rectangular sections with an aspect ratio of 2 and larger. They focused their investigation on the impinging shear layer instability, which was found to be responsible for vortex excitation for large aspect ratios (> 2). More recently, Deniz & Staubli (1997) studied the forced oscillations of a similar rectangular cylinder at intermediate Reynolds numbers, 64 000–160 000. They reviewed the different morphologies of the vortex shedding, which are reported in Fig. 4. They also presented some measurements of the phase angle between force and displacement and particularly, they detected an abrupt change of the phase angle between force and displacement in the lock-in range. This phenomenon was also reported for other cross-sectional shapes (Bearman & Obasaju 1982; Ongoren & Rockwell 1988).

More recently, Van Oudheusden (2000) studied the rotational galloping of a rigid cylinder having a rectangular section with an aspect ratio of 1.6. The experimental set-up allowed the cylinder to oscillate with a movement close to that of a pendulum, i.e., a rotational oscillation. One of the conclusions is a disagreement between quasi-steady theory and experiments in the estimation of the aerodynamic damping, which was found to be the main parameter governing galloping instabilities.

Another important point is the influence of the upstream turbulence especially to make the results more relevant to practical situations. A number of papers have been published on this. The pioneering work of Gartshore (1973) was the first to report on the effect of turbulence on galloping of rectangular cylinders. This effect was also studied in Novak & Tanaka (1974). Some of the other work is devoted to larger shape ratios (Li & Melbourne 1995; Matsumoto 2000) or to smaller ones (Nakamura & Ohya 1983, 1984; Saathoff & Melbourne 1999). For large shape ratios, it was shown (Haan *et al.* 1998) that the flow reattaches earlier when the intensity of turbulence is increased.

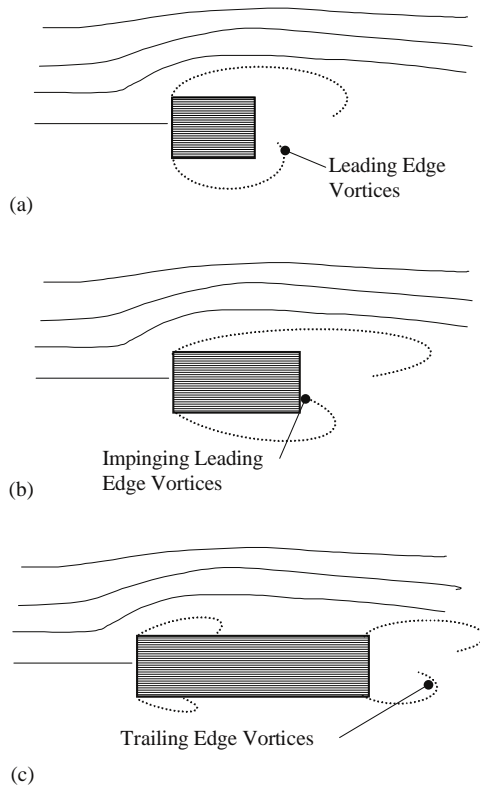


Figure 4. Morphology of the vortex shedding for different aspect ratios: (a) leading-edge vortices (LEV) when $c/e < 2$ to 3; (b) impinging leading-edge vortices (ILEV) when $2-3 < c/e < 5-9$; (c) trailing edge vortices (TEV) when $c/e > 5-9$.

The work presented in Matsumoto *et al.* (1998) is devoted to the study of large variations of the angle of attack α of rigid and flexible (clamped–free) rectangular models, between 0 and 90° in steps of 15°. However, the range of small values of the angle of attack, $< 10^\circ$, shows many different kinds of behaviour, and this region should be investigated more accurately.

Most of the dynamic studies are related to a pure lock-in phenomenon or to galloping of a rigid cylinder which can move perpendicularly to the main flow. The galloping theory proposed by Novak (1969) includes the effect of the vibration mode shape, using a nonlinear quasi-steady approach, but the experiments were also conducted for a cantilevered cylinder. As far as we know, and apart from the studies of Matsumoto and Novak both of whom used a cantilevered cylinder, the effect of real bending modes of a clamped–clamped cylinder has not really been studied. Such a cylinder has many bending modes that can interact with the flow, a mechanism that is not reported in the existing literature.

Thus, the experimental part of the present paper is devoted to the study of the behaviour of clamped–clamped cylinders, mainly for a rectangular section. We chose an aspect ratio of $c/e = 2$, because turbulence intensity is an important parameter with regard to galloping by varying the flow configuration from fully separated [as in Fig. 2(a)] to reattached [Figure 2(b)].

In the numerical simulations of this study, the Reynolds number range is that of the experiments, and it is higher than in the other numerical studies mentioned above.

Moreover, the differences between fixed and oscillating cylinders are not well documented, especially the wall pressure distributions, although the analysis of these data should lead to a better understanding of the aeroelastic phenomena.

2. METHODS OF INVESTIGATION

2.1. EXPERIMENTAL TOOLS

2.1.1. The wind tunnel

The tests were carried out in a small Eiffel-type wind tunnel of the Institut Aérotechnique. The square test-section has a width D of 0.6 m and a length of 2 m. Velocity can vary from 4 to 30 m/s, with a measurement accuracy of 1%. A single-channel hot wire anemometer was mounted for turbulence and wake investigations. Its nonlinear calibration curve is a fourth-order polynomial, and leads to an accuracy of 5%. Data acquisition was performed on a PC using a high-speed A/D converter with a sampling frequency up to 70 kHz.

The turbulence intensity I in the standard configuration is between 0.4 and 0.5% as shown in Fig. 5. The corresponding longitudinal correlation length (L_x) was calculated using the Taylor hypothesis on the basis of measurements of the integral time scale.

For the range of velocities 4–17 m/s of the present study, L_x is greater than the thickness of the rectangular cylinder and L_x/e is found to be in the range of 5–8. The corresponding time scale of the turbulence is smaller than the vibration period of the cylinder (1/27 s, see the next section), with a ratio between 0.1 and 0.05.

In order to generate turbulence, a square grid was mounted at the beginning of the test-section. This grid was inspired from Nakamura & Ohya (1983) and Hinze (1975). The mesh size $M = 60$ mm and is made up of 9 mm square rods. The lateral size of the test-section is then $10M$, and the longitudinal positions x/M investigated were 10, 13, 16, 19 and 22. The resulting turbulence intensities were respectively 7.5, 6, 5, 4.5 and 4% as is presented in Fig. 6.

The time macroscale was measured using two methods and measuring systems: (i) with the autocorrelation function obtained after a long averaging time by a real-time spectrum analyser, and (ii) the power spectrum at zero frequency. The results were consistent. The

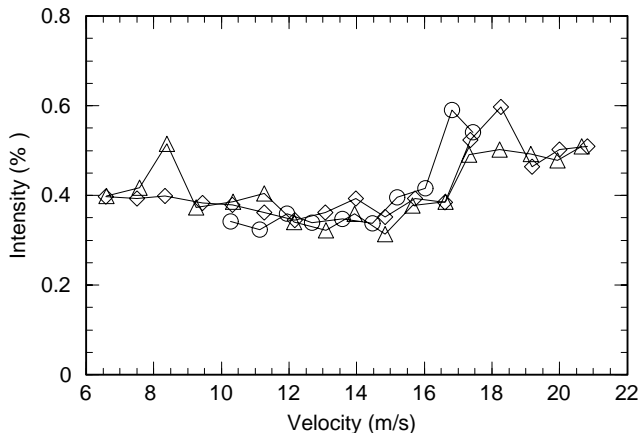


Figure 5. Turbulence intensity versus wind velocity for the smooth-flow configuration.

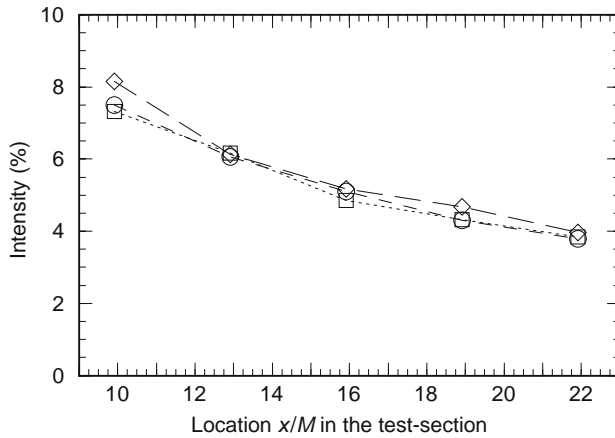


Figure 6. Turbulence intensity versus locations x/M in the test-section for different lateral positions: \circ , $y/D=0$ (middle); \square , $y/D=-1/6$; \diamond , $y/D=-1/3$.

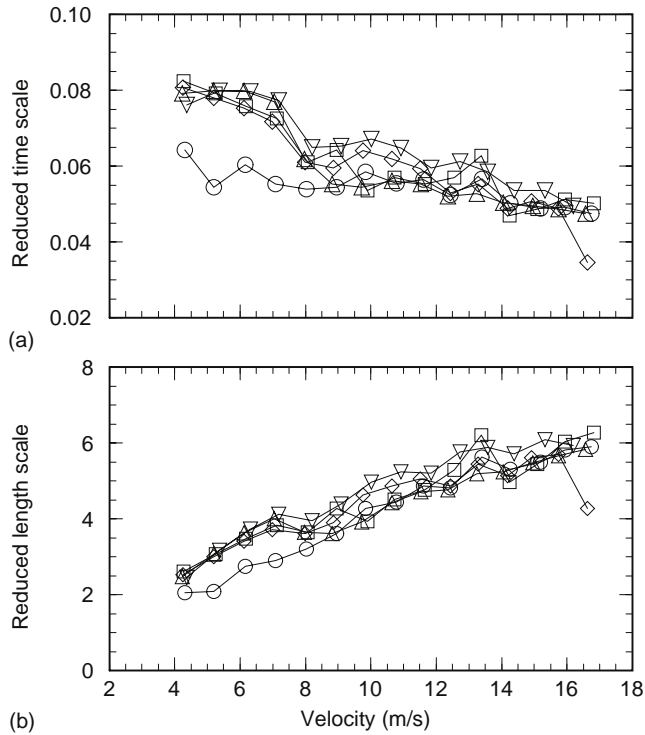


Figure 7. (a) Reduced time macro scale; (b) reduced length macroscale versus wind velocity at different locations x/M in the test-section. \circ , $x/M=9.92$; \diamond , $x/M=12.92$; \square , $x/M=15.92$; \triangle , $x/M=18.92$; ∇ , $x/M=21.92$.

time scale reduced by the first period of vibration of the rectangular model ($1/27s$) is given in Fig. 7. One may note that this time scale is smaller than the period of vibration.

By using Taylor’s hypothesis of isotropic and homogeneous turbulence, the longitudinal macroscale L_x is deduced and plotted in Fig. 7. It is reduced by the thickness e of the rectangular beam model. It should be noticed that the regime seems to be the same with

and without the grid because L_x/e is found in the range 2–6 in the turbulent case, which has to be compared to the range 5–8 for the smooth-flow configuration. Hence, the size of the turbulent eddies is only just greater than the size of the cylinder chord. The study focuses on the effects of the turbulence intensity and Table 1 presents a synthesis in physical units of the turbulence characteristics described above.

2.1.2. The vibrating model

The model tested is a beam clamped at both ends (Fig. 8). The dimensions of the rectangular section are $c=10$ mm, $e=5$ mm and its length is 950 mm. It is made of aluminium alloy and its first bending frequency is 27.3 Hz. The square-section cylinder is a tube with an external section of 8×8 mm and a thickness of 1 mm. The first bending mode has a frequency of 54.5 Hz. The clamping system was specially designed in order to obtain “ideal clamping” and to allow a variation of the angle of incidence ($\pm 30^\circ$). The finite element computation of the eigenfrequencies gave results in very good agreement with the measurements, the difference being $< 1\%$.

The free vibrations were measured using piezoelectric sensors glued to the beam. These consisted of $40 \mu\text{m}$ thick PVDF film glued to the middle upper face of the beam. It was connected to the acquisition system through a charge amplifier and an analog filter. The charge amplifier was wired so as to deliver a dynamic signal representing the velocity of the structure at the location of the sensor; thus the signal voltage was zero when the beam was not moving. This measuring method was chosen in order to eliminate zero shift problems due to thermal or pre-stress effects which are critical points when using piezoelectric techniques. However, the calibration of such a system is more complex since it needs to be done dynamically. A mass was suspended from the beam and then allowed to fall. The free

TABLE 1
Characteristics of the turbulence in the wind tunnel at $V=10$ m/s

Position x/M	Intensity (%)	Time macro-scale (s)	Longitudinal scale L_x (m)
16 (without grid)	0.4	0.0037	0.037
10	7.5	0.0022	0.022
13	6.0	0.0022	0.022
16	5.0	0.0022	0.022
19	4.5	0.0022	0.022
22	4.0	0.0022	0.022

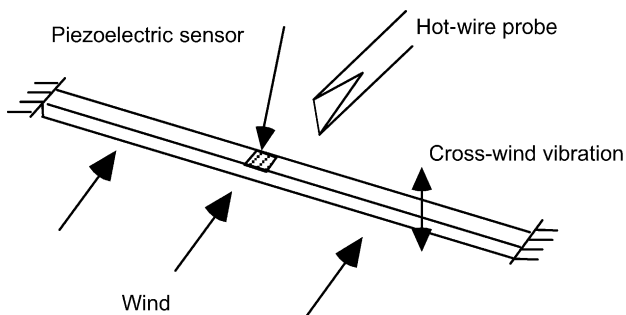


Figure 8. Principle of the wind tunnel tests.

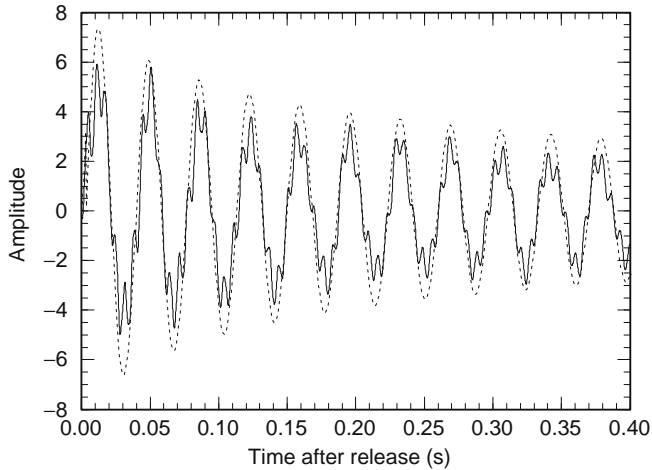


Figure 9. Dynamic calibration results: experimental and simulation (dotted line) curves.

damped vibrations were picked-up by the piezoelectric sensor. The reference solution was given by a finite element computation using a Timoshenko beam model. Fig. 9 gives an example of calibration results after introducing the structural damping and the calibration coefficient of the piezoelectric sensor. The global uncertainty on the amplitudes measured by the piezoelectric sensor was estimated to be of the order of 5%.

It should be noted that the system measures the response of more than one eigenmode, whereas the numerical solution is based on the first mode only. This is due to the fact that the sensor has a nonnegligible spanwise size, which is not the case for the reference signal given for a node of the finite element discretisation. There is also a well-identified perturbation at 50 Hz.

Measured structural damping is 0.24% of the critical damping for the rectangular section (0.85% for the square) and leads to a Scruton number of 22.6 (18.4 for the square). It was also noted that the damping was nonlinear for large amplitudes, as in a Van Der Pol oscillator. This is due to the mechanical system of insulation which absorbs the vibrational energy when it becomes high. After different calibration tests with different mass loads, it was found that a cubic term fits the experimental data well, using a nonlinear damping coefficient η_1 as in equation (2):

$$m\ddot{z} + 2(\eta + \eta_1 \dot{z}^2)\omega m \dot{z} + m\omega^2 z = 0, \quad (2)$$

where m , η and ω are the mass per unit length, the reduced damping and the angular frequency of the movement.

In this paper, the reference length is normally taken as the thickness e of the beam (5 or 8 mm). However, the Reynolds number of the tests is as usual based on the chord length c , and is in the range (5000–10000).

In what follows, the vibration results are given for the middle of the beam as the dimensionless oscillation velocity in the z direction (see Fig. 1) versus the reduced wind velocity. The reference frequency is the first bending frequency f of the cylinder (27 or 54 Hz). The amplitude of the velocity is the root-mean-square value (r.m.s.) of \dot{z} which, in practice, represents around 71% of the maximum value. Table 2 summarises clearly the main characteristics of the two models.

TABLE 2
Characteristics of the two cylinder models

Section	Chord c (mm)	Thickness e (mm)	Aspect ratio c/e	First bending frequency (Hz)	Damping ratio η (%)	Nonlinear damping η_1	Scruton number Sc
Square	8	8	1	54.5	0.85	3.5	18.4
Rectangular	10	5	2	27.3	0.24	0.8	22.6

2.2. NUMERICAL TOOLS

2.2.1. Navier–Stokes solver

The flow around a slender rectangular cylinder in cross-flow is approximated by a 2-D flow. As the focus is on low-frequency oscillations, in the first bending mode of the beam, a 2-D model of the vibrating cases is formulated; although 3-D effects are possible, they are neglected. Indeed, the largest coherent structures involved in the aeroelastic problems are widely known to have mainly 2-D characteristics: when a cylinder moves normal to the flow, the spanwise correlation of wall pressures increases, and therefore a 2-D approach is a good compromise (Tamura *et al.* 1993).

For the numerical simulations, we consider only a smooth flow at zero angle of attack ($\alpha=0$). The physical model is formulated with the full incompressible 2-D Navier–Stokes equations. One of the aims of the numerical simulations is to provide unsteady wall pressures around the structure, which will be processed with a proper orthogonal decomposition (POD) method and analysed in terms of frequencies; therefore, no turbulence modelling is added. In equations (3) the physical variables, the velocities u and the pressures p , are dimensionless:

$$\partial_t u + u \cdot \nabla u - \frac{1}{\text{Re}} \Delta u + \nabla p = 0, \quad \nabla \cdot u = 0; \quad (3)$$

Re is (similar to) the Reynolds number. The solver is based on a Lagrangian–Galerkin method. A mixed variational formulation of these full equations is implemented, with a finite element approximation for space discretisation (Girault & Raviart 1986). The convective problem is treated using a characteristic method, while the Stokes step is processed by an implicit algorithm (Pironneau 1989). Low-order characteristic methods are known to be diffusive on a large mesh, but the region of interest (around the structure) is discretised, so that a first-order derivative approximation with a fractional step characteristic method can be used.

The computations are carried out on geometry, Reynolds number and oscillation frequencies respecting the experimental conditions, particularly in the case of galloping. However, the numerical simulations consider forced oscillations of the structure, normal to the flow. Since the movement is that of a rigid body, the vibrations of the structure are simulated by applying the movement on the external boundary conditions. The computations are then performed in the reference frame of the body, and the grid acceleration term is taken into account in the equations.

The forced oscillation is a sine function

$$z(t) = z_{\max} \sin(2\pi f_r t_r), \quad (4)$$

where the imposed reduced velocity V_r (the inverse of f_r) is equal to 110. The amplitude z_{\max} is chosen to be equal to $c/\pi\sqrt{2}$, which corresponds to a

typical experimental value of

$$\sqrt{\bar{z}^2}/ef = 2 \quad (5)$$

as in Fig. 16 and assuming that the maximum value is $\sqrt{2}$ times the r.m.s. value.

2.2.2. The mesh

Without turbulence modelling, the scales of the simulated phenomena depend strongly on the mesh. A direct numerical simulation of all the turbulent scales for the studied Reynolds number, typically 6000, requires a mesh element area of approximately 2.15×10^{-6} , computed by $(\text{Re}^{-3/4})^2$, which cannot reasonably be done.

For the mesh selection, a criterion was used based on the quadratic error of the unsteady aerodynamic forces. The mesh was refined until this error was $<4\%$ of the lift force. Finally, a grid composed of 28 258 elements and 14 299 nodes was chosen. The minimal element size is 9×10^{-6} , and 300 nodes are located on the wall of the structure (see details in Fig. 10).

Fig. 11 shows the sensitivity of the mesh to the aerodynamic coefficients. We note the single sine wave of the lift, obtained by resolution on the coarse mesh, which corresponds to a smaller Reynolds number as in Davis & More (1982).

2.2.3. The proper orthogonal decomposition

The POD is a powerful method for analysing unsteady components in aerodynamics (Holmes *et al.* 1996), and for detecting coherent structures. By comparison with the vorticity visualisations, the POD has the advantage of analysing the physical components in space and in time. It is then a good method for problems in aeroelasticity (Dowell *et al.*, 1999).

The essence of the POD technique is that it is a method of decomposition which uses arbitrary orthogonal functions that have to be determined. It is currently used for reducing the order of models to solve flow problems, or for the post-processing of data and analysis, which is the case here. It can be viewed as a more general method than the Fourier or wavelet analysis, because the base functions are not chosen a priori. It is also called the principal components analysis by statisticians (Lebart *et al.* 1982).

The method is based on the Karhunen–Loève decomposition of a multivariable signal. The main idea is to find a set of proper orthogonal functions that capture the maximum of the energy of the signal with the minimum number of proper functions.

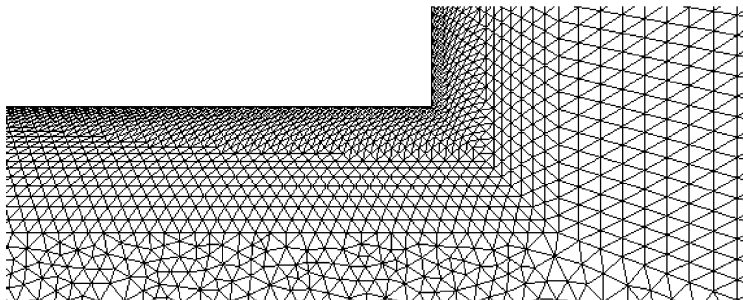


Figure 10. Mesh used in the numerical simulations (detail of the lower right corner of the cylinder).

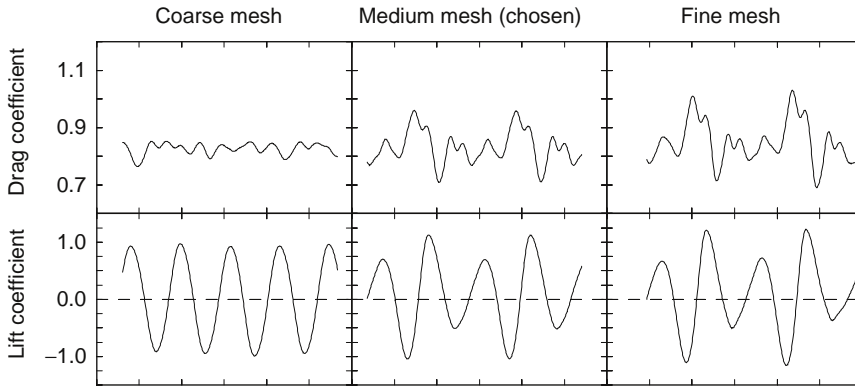


Figure 11. Drag and lift coefficients computed with three different meshes.

In the present case, the POD is applied to the wall pressure distribution $\mathbf{P}(\mathbf{X},t)$ around the structure which can be written as

$$\mathbf{P}(\mathbf{X}, t) = \sum_n \mu_n(t) \mathbf{W}_n(\mathbf{X}), \tag{6}$$

where the proper functions \mathbf{W} are the eigenvectors of the two-point correlation matrix \mathbf{R}_c of the pressure distribution. The optimisation problem of the Karhunen–Loève decomposition is then reduced to an eigenmode problem:

$$\mathbf{R}_c \mathbf{W} = \lambda \mathbf{W}, \tag{7}$$

where the eigenvalues λ can be seen as representative of the relative energy levels. The convergence is theoretically optimal which will be confirmed in practice.

Problem (7) is solved numerically by the subspace method of Bathe and Wilson. The size of this problem is given by the number of nodes over the cylinder and is 300×300 , as mentioned previously. The nodes on the wall were uniformly distributed and no correction as suggested in Jeong *et al.* (2000) was applied.

For the present application, it is really interesting to estimate the contribution of each proper function to the component of the aerodynamic forces by using, for the lift coefficient,

$$C_{z_n}(t) = \frac{\mu_n(t) \langle \mathbf{W}_n, \mathbf{n}_z \rangle}{\rho V^2 / 2}, \tag{8}$$

where \mathbf{n}_z are the z components of the normal vectors of the structure, the symbol $\langle \rangle$ denoting the space integration over the surface of the cylinder. The principal components are given by

$$\mu_n(t) = \langle \mathbf{P}(\mathbf{X}, t), \mathbf{W}_n \rangle, \tag{9}$$

when the normalisation procedure of the proper functions is chosen, so that

$$\langle \mathbf{W}_n, \mathbf{W}_n \rangle = 1. \tag{10}$$

Anyhow, the sum of all the contributions to the force are equal to the total force, which gives for the lift

$$C_z(t) = \langle \mathbf{P}(\mathbf{X}, t), \mathbf{n}_z \rangle = \sum_n C_{z_n}(t). \tag{11}$$

Equations (8) and (11) can easily be extended to obtain the drag and pitching coefficients by projecting onto the x components of the normal vector.

From the classical properties of the eigenmodes (orthogonality and normalisation), it is easy to show that the mean-square of the principal components is equal to the eigenvalue,

$$\overline{\mu_n^2} = \lambda_n, \tag{12}$$

with the overbar denoting time integration. Also, the total mean-square of the pressure distribution is equal to the sum of the eigenvalues, i.e.,

$$\sum_i \overline{p_i^2} = \sum_n \lambda_n. \tag{13}$$

Hence, it is possible to express each eigenvalue with reference to its sum, usually as a percentage, so as to obtain a good indicator of the efficiency of the decomposition by making the cumulative sum. However, for the purpose of the present application, it is also important to define an unbiased quantity which could allow the classification of the proper functions by reference to the different aerodynamic force components. Indeed, the eigenvalues are the global indicators of the energy of each proper function with respect to the total energy in the pressure distribution; however, their decomposition into force components is not immediately available.

Next, we introduce a projection of the mean-square value of the force component onto the corresponding eigenvalue:

$$\overline{C_{z_n}(t)^2} = \lambda_n \left(\frac{\langle \mathbf{W}_n, \mathbf{n}_z \rangle}{\rho V^2 / 2} \right)^2. \tag{14}$$

Indeed, the properties of the eigenvectors and equations (8) and (12) induce the orthogonality of the family (C_{z_n}) for the time integration, i.e.,

$$\overline{C_{z_n}(t)C_{z_m}(t)} = \lambda_n \left(\frac{\langle \mathbf{W}_n, \mathbf{n}_z \rangle}{\rho V^2 / 2} \right)^2 \delta_{nm}, \tag{15}$$

where δ_{nm} is the Kronecker symbol. This leads to

$$\overline{C_z(t)^2} = \sum_n \overline{C_{z_n}(t)^2}. \tag{16}$$

As for the eigenvalues, a new coefficient is introduced as a proportion of the contribution of each proper function to the mean-square component of the aerodynamic force, which is defined by

$$EC_{z_n} = \frac{\overline{C_{z_n}(t)^2}}{\overline{C_z(t)^2}} \tag{17}$$

and usually given as a percentage. This coefficient is also defined for the drag force and the pitching moment within the same procedure.

2.2.4. The mean-value problem

The POD can be performed on data which have a mean component, This is a major difference to the wavelet method, as notably pointed out in Farge (1992). Moreover, in the case of aerodynamic quantities, the analysis can be performed on the total component (static + fluctuating), which is much more interesting for applications in aeroelasticity.

A contrario to some authors using the POD, experience shows that there is no “true eigenvector” as claimed by Tamura *et al.* (1999), but there are only some eigenvectors useful for the physical analysis of the problem. Thus, the choice of including or not the

mean value in the correlation matrix cannot be made from the result of a rigorous mathematical demonstration. The only proven result is that the eigenvectors found will be different in the two cases. Because the purpose of POD is only data analysis, the arguments for including or not the mean component is decided by the particular application and for a specific use of the results. For example, the application on domes by Letchford & Sarkar (2000) leads to interesting physical interpretations with the mean value included in the pressure signals.

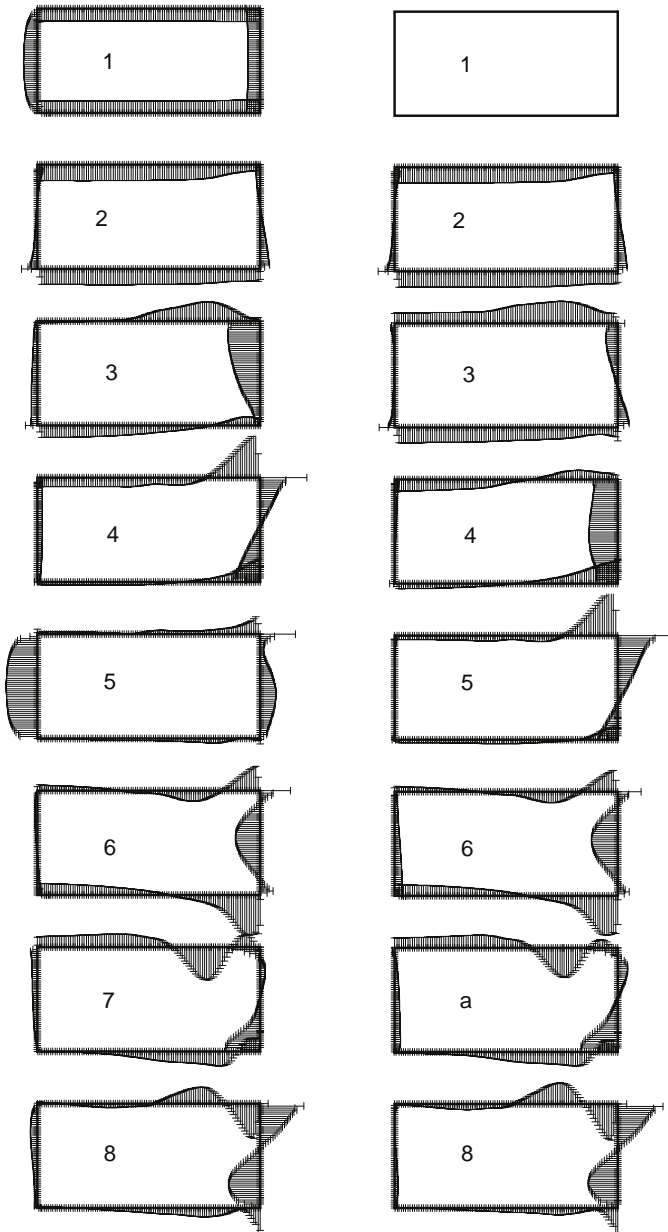


Figure 12. Proper (POD) functions with (left) and without (right) inclusion of the mean value.

Moreover, insofar as we are interested here in an aeroelastic problem which contains nonlinearities in the aerodynamic forces, the exclusion of the mean value would implicitly assume a linearity of the problem, because the mean level, at which the phenomenon occurs, would not be taken into account. However, even if the POD is a linear operation, it does not need and does not assume linearity of the process which is studied. In other terms, this means that nonlinear phenomena in the original signal will be transferred into the decomposed signal without modification. Consequently, there are some difficulties in making comparisons between the two kinds of decomposition when the phenomena are not at a zero mean value.

In order to illustrate this point, and before presenting all the results in detail, a POD has been made for the case of the nonvibrating rectangular cylinder with and without inclusion of the mean value. Fig. 12 presents the comparison between the results that include or not the mean value for the eight first proper functions around the rectangular cylinder, with the wind coming from the left. It will be shown in the next sections that these eight functions are sufficient for the analysis of the aerodynamic forces. In order to make the comparison easier, the number of modes for the case that excludes the mean value has been increased by one, since the first mode should represent the mean component. Only two proper functions do not correspond (3 and 5 with the mean value, and 3 and 4 without), because they are both strongly related to the drag force which is not a zero mean-value mechanism. The other functions are similar; therefore all the PODs presented hereafter will include the mean value, because it is more convenient for the recombination of the aeroelastic forces which we are interested in. This point remains, however, under discussion and requires further investigations especially for non-Gaussian signals.

3. RESULTS

In this section we present the results of the experiments with the square and rectangular cylinders at different angles of attack as well as the numerical simulations with the rectangular section at $\alpha = 0$. The experimental study of the effects of the upstream turbulence was conducted with the rectangular cylinder. The configurations that were studied are summarised in Table 3, where the differences between VIV and MIV refer to the corresponding reduced velocity ranges.

The numerical simulations, in smooth flow, were only performed on the rectangular section at zero angle of attack for the static case and for galloping (MIV) at $V_r = 110$.

TABLE 3
Configurations studied

Section	Type of aeroelastic excitation	Experiments		Numerical simulations	
		Turbulence intensity	Angle of attack	Turbulence intensity	Angle of attack
Square	Static	0.5%	0–30°	–	–
	VIV	0.5%	0–15°	–	–
	MIV	0.5%	0–15°	–	–
Rectangular	Static	0.5–7.5%	0–30°	smooth flow	0°
	VIV ($V_r \approx 60$)	0.5%	0–6°	–	–
	MIV	0.5–7.5%	0–6°	smooth flow	0°

3.1. STATIC CASE

3.1.1. Rectangular section

The aerodynamic forces (drag, lift and pitching moment) obtained numerically are given in Fig. 13 versus the reduced time t_r (the label $C_z(2)$ will be explained later in Section 4.1) and in Fig. 14 versus the reduced frequency f_r (magnitude of the Fourier transform, dimensionless quantity such as a force coefficient).

The statistical results are given in Table 4. The mean drag coefficient 0.82 is in good agreement with the results reported in Norberg (1993) which gives 0.80. Also, Deniz & Staubli (1997) gives 0.70 but for an experiment at a higher Reynolds number, whose effect is known to produce a lower drag force due to an earlier reattachment of the shear layers (Nakamura & Ohya 1983).

Also, the Strouhal number was measured versus the angle of attack with various intensities of turbulence and the results are given in Fig. 15(a). These measurements were performed with the cylinder kept fixed. At zero angle of attack, the computed Strouhal number (0.086), given by the fundamental frequency of the lift coefficient (see Fig. 14), compares well with the experiments in smooth flow (0.085). These results are also in agreement with those of many other authors (Norberg 1993; Matsumoto *et al.*, 1998; Deniz & Stabuli, 1997). It must be pointed out that the reference length used for the computation of the Strouhal number always remains the thickness of the cylinder, and is not modified by the angle of attack, as sometimes done by others authors.

For smooth flow at 0° , the Strouhal number is due to impinging leading-edge vortices. The jump at an angle between 4 and 6° is linked to a change in the pure shedding of

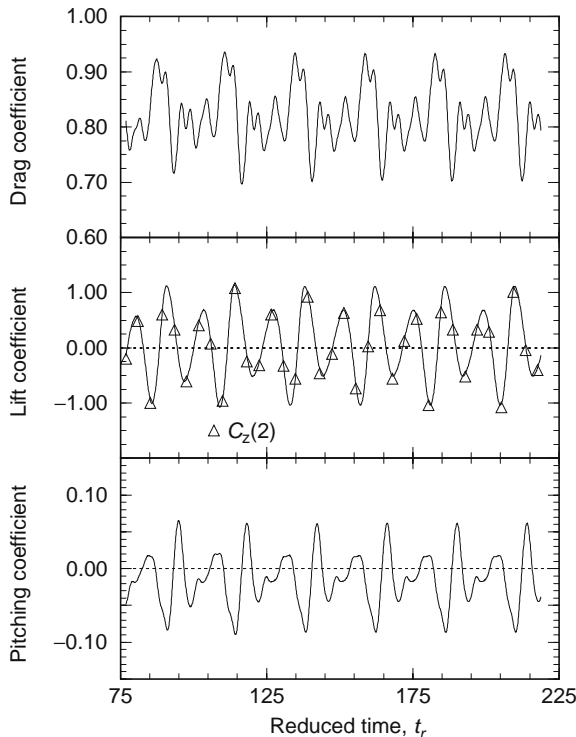


Figure 13. Computed time histories of aerodynamic forces: rectangular section, $\alpha=0^\circ$, smooth flow, $Re=6000$, nonvibrating.

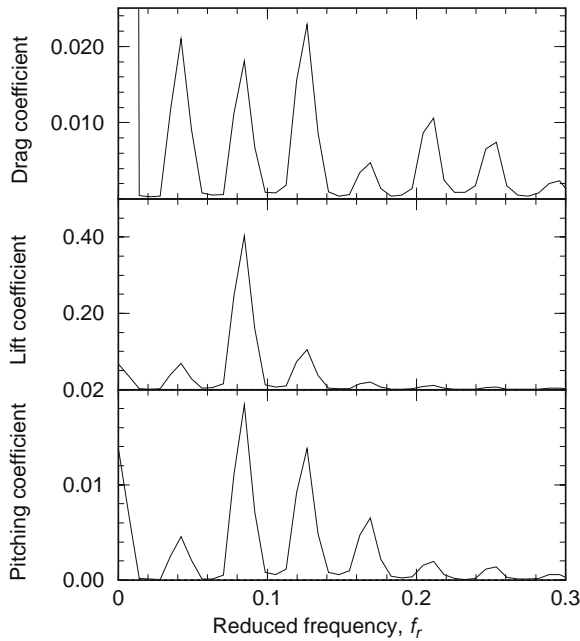


Figure 14. Computed Fourier transforms of aerodynamic forces: rectangular section, $\alpha=0^\circ$, smooth flow, $Re=6000$, nonvibrating.

TABLE 4

Statistical results of the aerodynamic forces. Rectangular section, $\alpha=0^\circ$, smooth flow, $Re=6000$, nonvibrating and galloping cases

	Component	Mean value	Standard deviation
Static case	Drag coefficient	0.82	0.056
	Lift coefficient	0.	0.60
	Pitching moment coefficient	-0.014	0.036
Gallopig, $V_r=110$	Drag coefficient	0.84	0.027
	Lift coefficient	0.0	0.75
	Pitching moment coefficient	-0.013	0.042

alternate vortices on the edges due to the geometrical effect of the angle of attack. The morphology of these vortices corresponds to one vortex which separates at the leading edge, and the other at the trailing edge (Deniz & Staubli 1997).

In turbulent cases, the peak in the power spectrum of the velocity was less dominant, and a longer averaging time was necessary, especially for the small angles of attack, because the impingement of the leading-edge vortices becomes less periodic with increasing turbulence. At the angles of $0-4^\circ$, the shedding is so irregular that it is not really possible to attach a meaning to the given Strouhal numbers, even if they correspond to a small peak in the velocity spectra.

Between 4 and 8° in turbulent flows, no significant peak could be detected which means that no coherent and periodic impinging leading-edge shedding occurred. For incidences $> 8^\circ$, smooth and turbulent flows produce the same results due to the alternate edge vortex shedding.

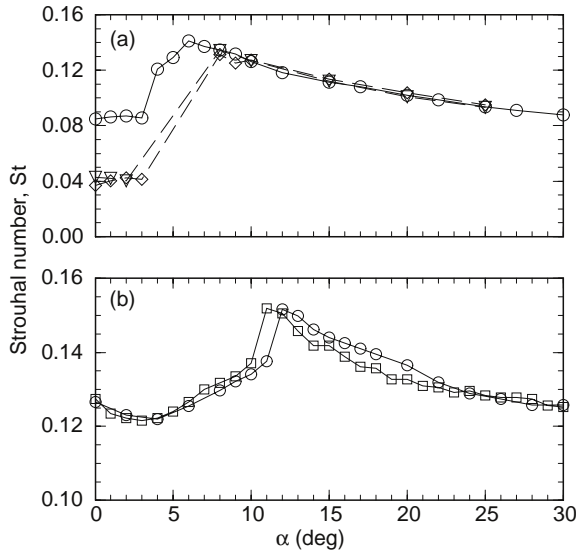


Figure 15. Measured Strouhal number versus angle of attack: (a) rectangular section, $Re = 6000$. \circ , $I = 0.5\%$; \diamond , $I = 4.5\%$; ∇ , $I = 6\%$ and (b) square section, smooth flow: \circ , $Re = 5000$; \square , $Re = 9000$.

Thus, these measurements confirm that the unsteady reattachment on the lateral sides is strongly influenced by free-stream turbulence. Unfortunately, there are no measurements at turbulence intensities between 0.5 and 4%, a range over which the Strouhal number changes radically. We do not really know whether this change is sudden or progressive. However, one may expect the turbulence to modify the flow regime (i.e., the morphology of the vortex shedding) abruptly.

3.1.2. Square section

This section was studied only in the wind tunnel and only in smooth flow. For the static case, the Strouhal number was measured and is plotted in Fig. 15(b) versus the angle of attack. The agreement with the results given by Luo *et al.* (1994) is very good.

The jump between leading-edge vortices and alternate-edge vortices occurs between 11 and 12° as the Reynolds number varies from 9000 to 5000. An increase in the Reynolds number produces an earlier jump that is classically linked to a decrease in the wake width.

3.2. THE VORTEX-INDUCED VIBRATION EXPERIMENTS

3.2.1. Rectangular section

The rectangular section was found to be sensitive to the alternate vortex-shedding within a particular mechanism which we describe in this section. The fundamental data are well summarised in Table 5 at zero angle of attack. The velocities at lock-in are deduced from the Strouhal number measured for the static case ($St = 0.085$). The reference frequency used for the dimensionless parameters, such as the reduced velocity, always remains that of the first mode.

Concerning the first mode, the velocity at lock-in is very low and cannot be obtained experimentally in the wind tunnel without instability of the flow due to the very low regime of the fan. Thus the excitation of this mode was only detected and it was not possible to make reliable measurements.

TABLE 5

Bending frequencies and corresponding velocities at lock-in. Rectangular and square sections, $\alpha=0$, smooth flow

Model	Bending mode	Frequency (Hz)	Lock-in velocity (m/s)	Lock-in reduced velocity
Rectangle	First	27.3	1.57	11.5
	Second	75.2	4.32	31.7
	Third	147.5	8.48	62.0
Square	First	54.55	3.43	7.87
	Second	150.0	9.45	21.65
	Third	294	18.5	42.5

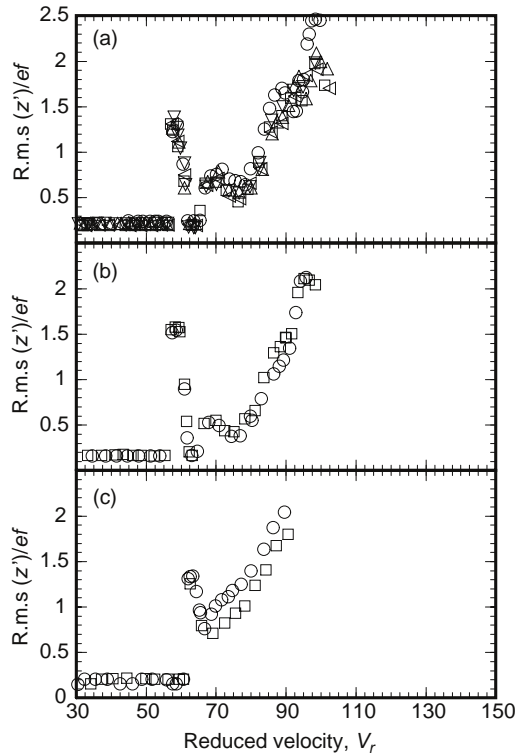


Figure 16. Vibrations results of rectangular section in smooth flow: (a) $\alpha=0^\circ$; (b) $\alpha=2^\circ$; (c) $\alpha=4^\circ$.

The second bending mode was not excited experimentally, although the velocity could be stabilised around the lock-in. In fact, this mode has the classical shape of a second bending mode, with one node in the middle and two antisymmetric maxima. Due to this shape, and because the wind profile along the span is constant, no wind excitation can occur. In other words, the modal mass of such an eigenmode being zero (Gérardin & Rixen 1993), its participation in the vibrations should indeed be negligible, which is found experimentally.

VIV occurred with lock-in for the third mode, at a velocity within the standard range of the wind tunnel. Lock-in occurred at a reduced velocity of 60, as can be seen in Fig. 16(a), which is close to the value of 62 given by the theory (Table 5). It must be pointed out that the computation error of the eigenfrequencies increases with their order, mainly because of

the effect of the inertia of rotation. Fig. 16(b), present the same kind of results for angles of attack of 2 and 4°.

However, this apparently standard lock-in evolves in a more complex manner, so that, in the end, the steady vibrations occur in the first mode, although the upstream wind velocity remains constant, i.e., that of the initial resonance with the third mode.

In fact, the behaviour before reaching steady vibrating conditions due to vortex shedding is quite complex. Indeed, the vibrations start in the third mode, due to the coincidence of frequencies; but as the amplitude grows, the movement is transferred onto the first bending mode, at a lower frequency. Finally, vibrations become well established in the first mode.

This transient process is difficult to observe and takes about 60 s. Nevertheless, in the final steady state, the shape of the first bending mode could be well observed using a stroboscope. Moreover, the Fourier analysis of the signal of the piezo-sensor actually showed a main frequency equal to that of the first mode, as shown in Fig. 17(a). This signal has not been filtered so as to be able to evaluate the contribution of harmonics, which are much smaller than the fundamental mode. Also, the longitudinal velocity in the wake (given by a hot-wire probe mounted downstream at a distance of two chords, c) presents a dominant frequency on the first mode of vibration, as can be seen in Fig. 17(b) (the two signals were acquired simultaneously).

The flow in the wake shows a well-established periodic component that is clearly linked with the vibration. The shedding of the vortices is triggered by the oscillations of the cylinder. The flow does not show any tendency to return to the regime of natural shedding, although the frequencies are really different (i.e., 27 Hz as compared to 147 Hz).

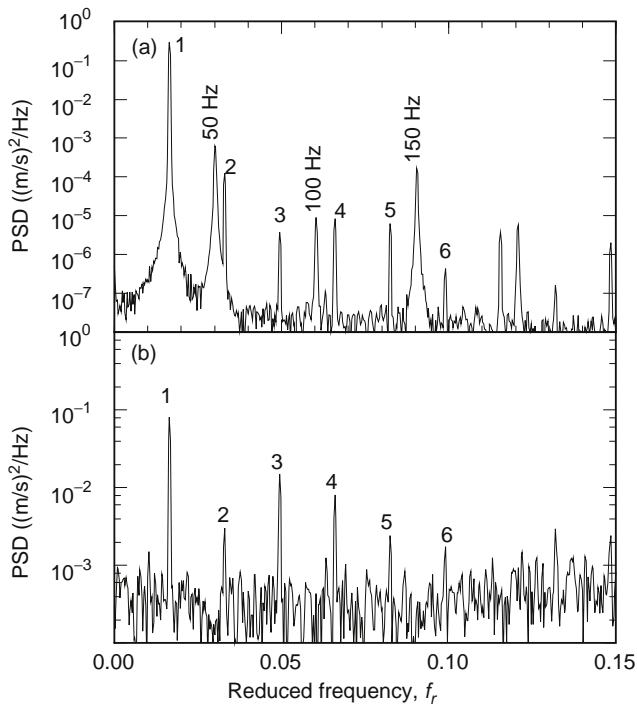


Figure 17. Power spectral densities of rectangular section, $\alpha=0^\circ$, smooth flow, $V_r=60$: (a) vibration velocity; (b) velocity in the wake.

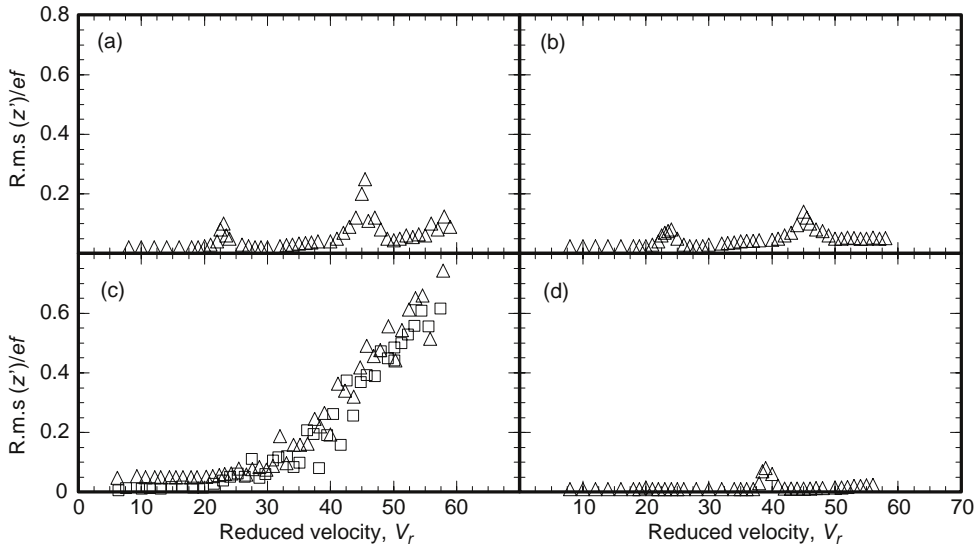


Figure 18. Vibration results of square section in smooth flow: (a) $\alpha=0^\circ$; (b) $\alpha=5^\circ$; (c) $\alpha=10^\circ$; (d) $\alpha=15^\circ$.

It is obvious that this phenomenon cannot occur with the rigid body considered in other studies. As far as we know, this may be the reason why it has not been reported before.

3.2.2. Square section

As for the rectangular section, Table 5 shows the possibility of lock-in for the square section estimated from the Strouhal number measured on a static cylinder ($St=0.127$). The vibration results are plotted in Fig. 18 for angles of attack of 0, 5, 10 and 15° . At 10° , the galloping instability is dominant and the vortex excitation is not visible although it is probably present.

The behaviour is very similar to that of the rectangular section, with the excitation of the third bending mode, at $V_r=44$ for $\alpha=0$ and 5° , and $V_r=39$ for $\alpha=15^\circ$. The amplitude is generally very small because the structural damping of this cylinder is larger; therefore, the accuracy of the amplitude of each peak is not very good and the analysis of steady vibrations is not reliable enough. Nevertheless, the behaviour is qualitatively similar to that of the rectangular cylinder.

Moreover, at 0 and 5° a small excitation peak exists at $V_r=22$, which seems to be a resonance of the third bending mode in the direction of the mean flow (all the bending modes are double because of the square section) coupled with the first harmonic term of the vortex shedding. This corresponds to twice the Strouhal number. The amplitude is very small, because here the sensor is not supposed to be sensitive to the displacement in the streamwise direction. This mechanism has been thoroughly studied by Obasaju *et al.* (1990).

3.3. GALLOPING CASE

3.3.1. Rectangular section

The galloping phenomenon occurs at larger reduced velocities than the vortex shedding excitation. This can be seen in Fig. 16 for the rectangular section in smooth flow at 0, 2 and 4° of angle of attack. At 6° , this section is stable in galloping.

The experimental results for turbulent flows are given in Fig. 19, where it can be seen that the galloping instability was not detected at 4° for reduced velocities below 150. The critical velocities at which galloping sets in are summarised in Table 6. It is interesting to note that the critical velocity first decreases when the turbulence increases and then increases until stability is reached when the turbulence is further increased.

The numerical simulations were performed in smooth flow with forced oscillations at $V_r=110$. The resulting time histories of the forces are given in Fig. 20 and the statistical values in Table 4. The coupling with the period of the movement is clearly visible on the aerodynamic coefficients. A kind of organisation of the flow occurs

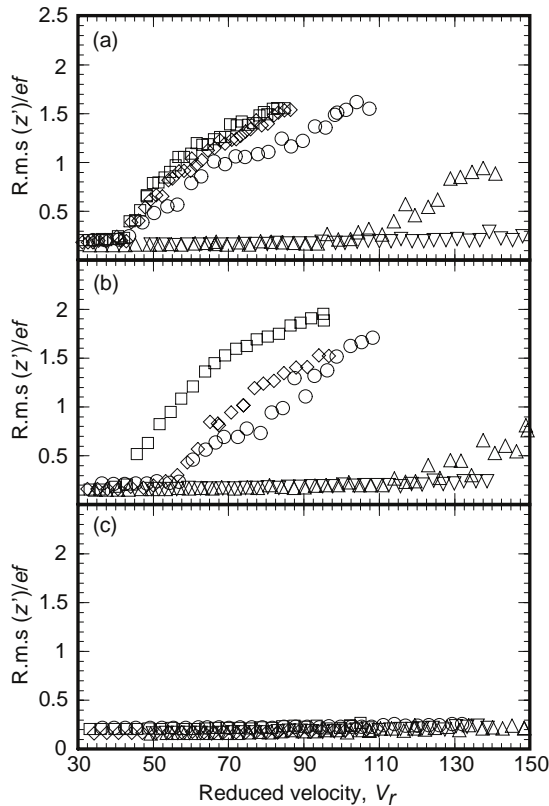


Figure 19. Vibration results of rectangular section in turbulent flows: (a) $\alpha=0^\circ$; (b) $\alpha=2^\circ$; (c) $\alpha=4^\circ$. \circ , $I=4\%$; \square , $I=4.5\%$; \diamond , $I=5\%$; \triangle , $I=6\%$; ∇ , $I=7.5\%$.

TABLE 6
Critical reduced velocities for galloping. Rectangular section

Turbulence intensity	$\alpha=0^\circ$	$\alpha=2^\circ$	$\alpha=4^\circ$	$\alpha=6^\circ$
0.5%	65	65	65	Stable
4%	42	55	Stable	Stable
4.5%	42	42	Stable	Stable
5%	42	55	Stable	Stable
6%	110	120–130	Stable	Stable
7.5%	Stable	Stable	Stable	Stable

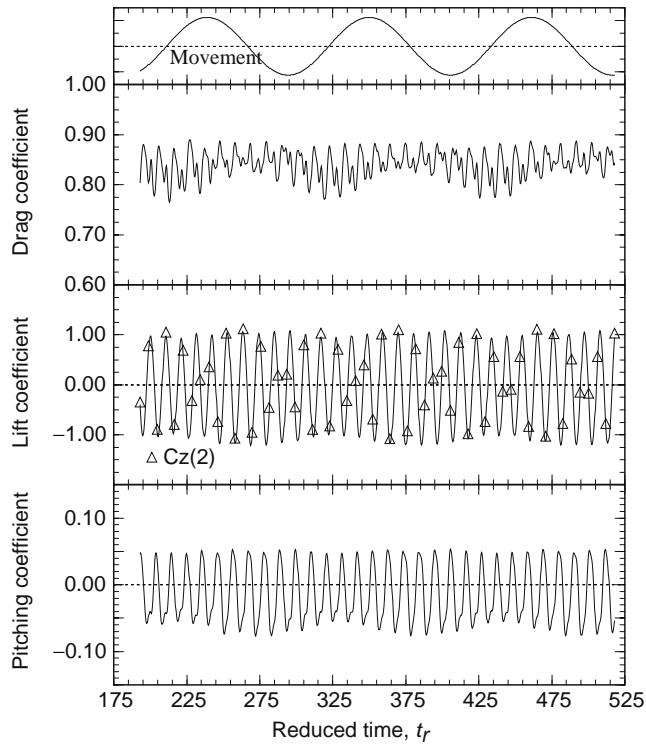


Figure 20. Computed time histories of aerodynamic forces: rectangular section, $\alpha=0^\circ$, smooth flow, $Re=6000$, $V_r=110$ (galloping).

because the time history of the lift becomes close to a simple sinusoid, as shown by the Fourier transform in Fig. 21.

In the experiments, when comparing the VIV and the MIV regimes, very few differences are present in terms of the dynamics of the measured signals on the structure, as can be seen in the spectra in Fig. 22 compared to Fig. 17. Indeed, the structural vibrations are completely similar, since the wake signal only detects the fundamental vibration of the beam, without the harmonics which are present in the VIV case. The vortices that are shed during galloping are clearly triggered by the vibration, whereas the shedding in the VIV case is naturally present and induces a lock-in.

3.3.2. Square section

This case was investigated less than the rectangular section, and galloping occurred only at an angle of attack of 10° , as can be seen in Fig. 18. For the small angles, 0 and 5° , galloping should have occurred at a higher velocity which cannot be obtained in the wind tunnel. Indeed, the negative lift slope C'_z at 0° is only -2.05 , whereas at 10° it is much higher, -8.16 , which explains why the critical velocity was not reached at 0° . The tests on this cylinder will find their use in the validation of the model proposed in the next section.

4. DISCUSSION AND ANALYSIS

The previous results are used in this section in order to better understand the problem of galloping vibrations through a more thorough description of the morphology of the

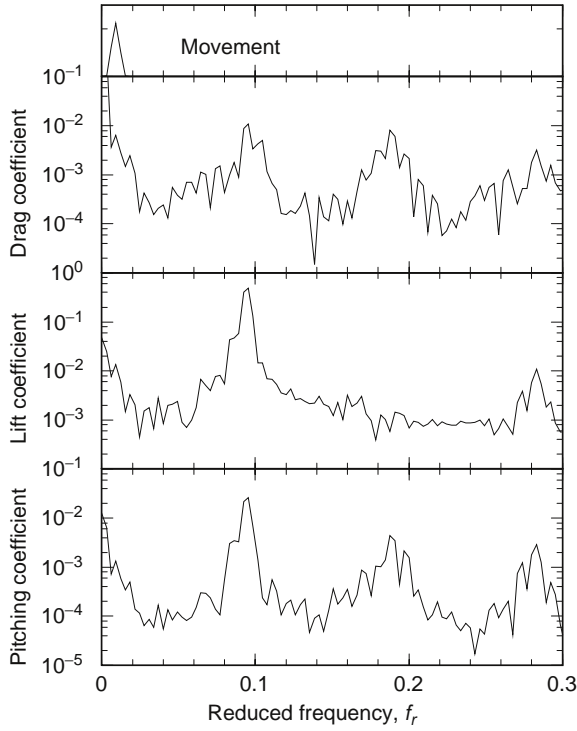


Figure 21. Computed Fourier transforms of aerodynamic forces: rectangular section, $\alpha=0^\circ$, smooth flow, $Re=6000$, $V_r=110$ (galloping).

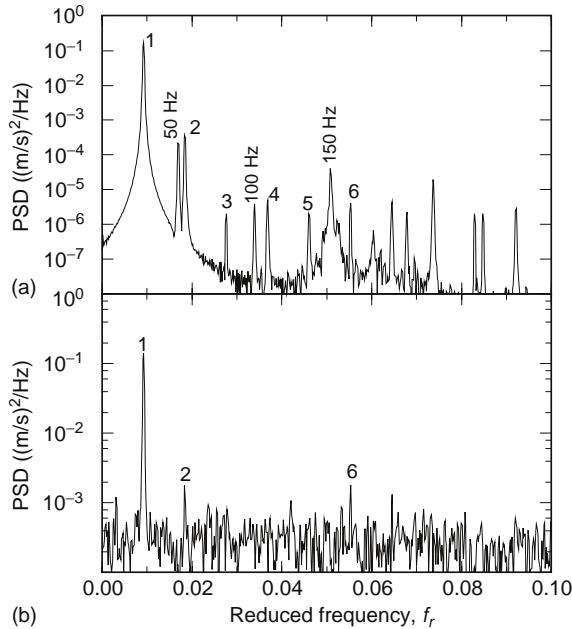


Figure 22. Power spectral densities of rectangular section, $\alpha=0^\circ$, smooth flow, $V_r=110$: (a) vibration velocity; (b) velocity in the wake.

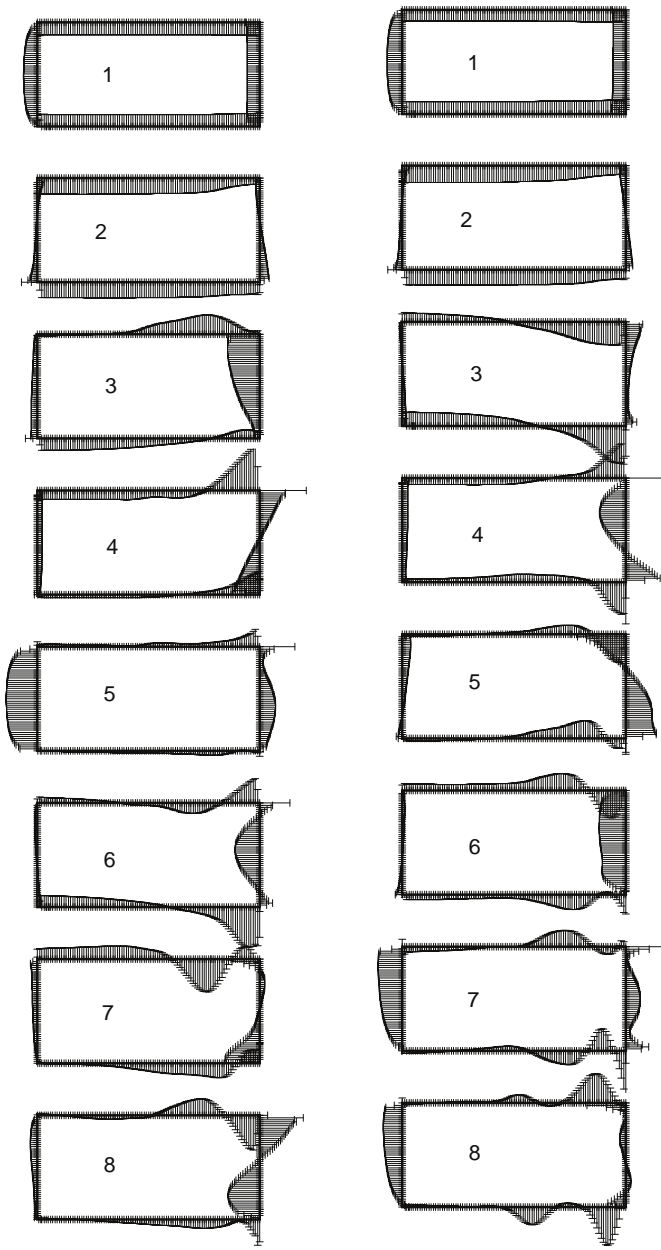


Figure 23. Proper functions in static (on left) and galloping cases (on right, at $V_r = 110$).

pressure loads on the cylinder, without and with oscillations. Then, as a second step, we propose an improvement to the quasi-steady theory that could better fit the experimental results.

4.1. ANALYSIS WITH THE PROPER FUNCTIONS

In order to analyse the components of the aerodynamic forces, the POD method described in Section 2.2.3 is applied to the computed results. The idea is to establish links between

the morphology of the proper functions (plotted in Fig. 23) that have some kind of universal shapes, and a physical view of the phenomenon.

The distribution of the eight largest eigenvalues is shown in Fig. 24; the other graphs in this figure show the distributions of the eigenvalue projections onto the force components [cf. equation (17)]. They give useful information for the interpretation of the proper functions.

The diagrams of Fig. 24 prove that the changes in the energy distribution of the proper decomposition are appreciable between the static case and galloping, and they are more visible for the projections onto the force components. Indeed, the proper functions themselves are modified; the shape of these functions (cf. Fig. 23) are different, some of them change in order, some disappear and others are modified or entirely new. So, it is difficult to compare the two regimes mode for mode.

It must first be noted that the second proper function is preponderant for the lift. This is verified by comparing the lift contribution of this function with the computed total lift (cf. Fig. 13 for the static case and Fig. 20 for the galloping case, where the two curves are superimposed); the contribution of the other modes is negligible. It is interesting to see here that the POD is a very efficient method for reducing the order of the data set, because only one function is necessary to recombine the lift

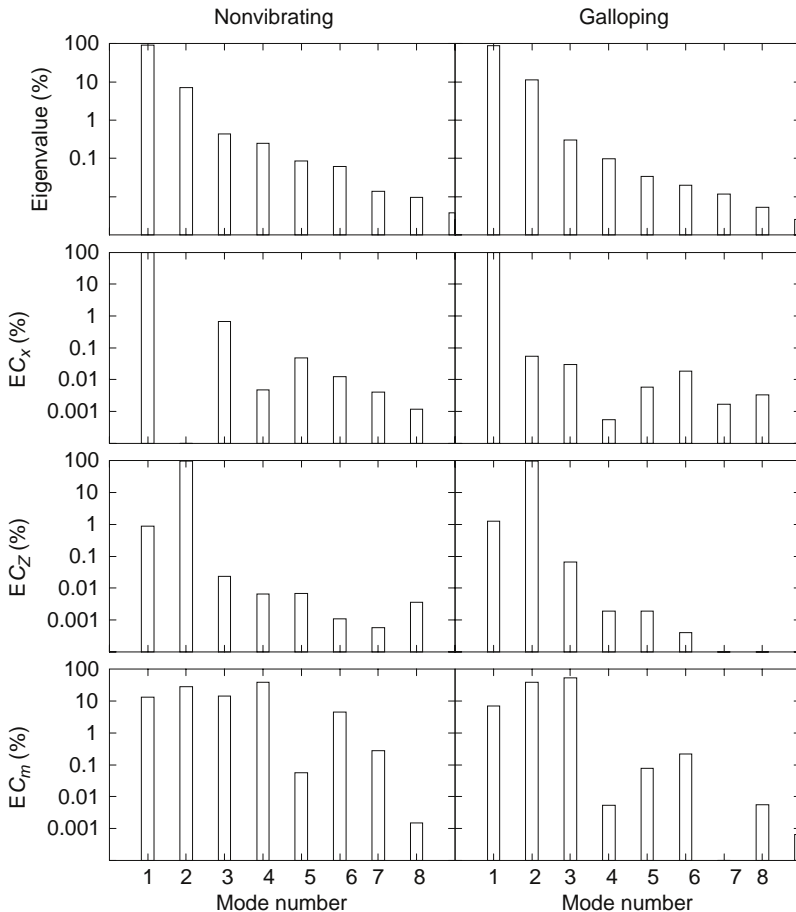


Figure 24. Eigenvalues and their projections onto the force components in static and galloping cases.

history, which remains one of the most important mechanical parameters for the aeroelastic behaviour.

For the drag, the first proper function, which contains the pressure mean value, is of course preponderant but the fluctuations caused by the contributions of the next six functions are necessary to obtain a good representation of the unsteady drag coefficient. We note that function 2 has a negligible contribution to the drag in the static case, which seems not to be the case in the galloping regime. In fact, one must remember that the quantities are percentages of the total mean-square value: the standard deviation of the drag component in the galloping case is almost half that of the static case (cf. Table 4). Thus, the absolute contribution of the fluctuations of the proper functions is smaller for the MIV case.

Time histories and corresponding spectra of contributions of each proper function are presented in Figs. 25 and 26 for the pitching moment. The same analysis could be done for the lift force; however, due to the location of the secondary vortices on the rear part of the chord, their effect on the pitching moment is amplified and therefore, this component is preferred for the analysis.

In the galloping case, the movement globally induces a reorganisation of the fluctuations of the low-order contributions due to the fact that the secondary vortices, located inside the shear layer, are made symmetrical instead of alternate, so that their effect on the global force component is cancelled. Indeed, in the static case, the unsteady

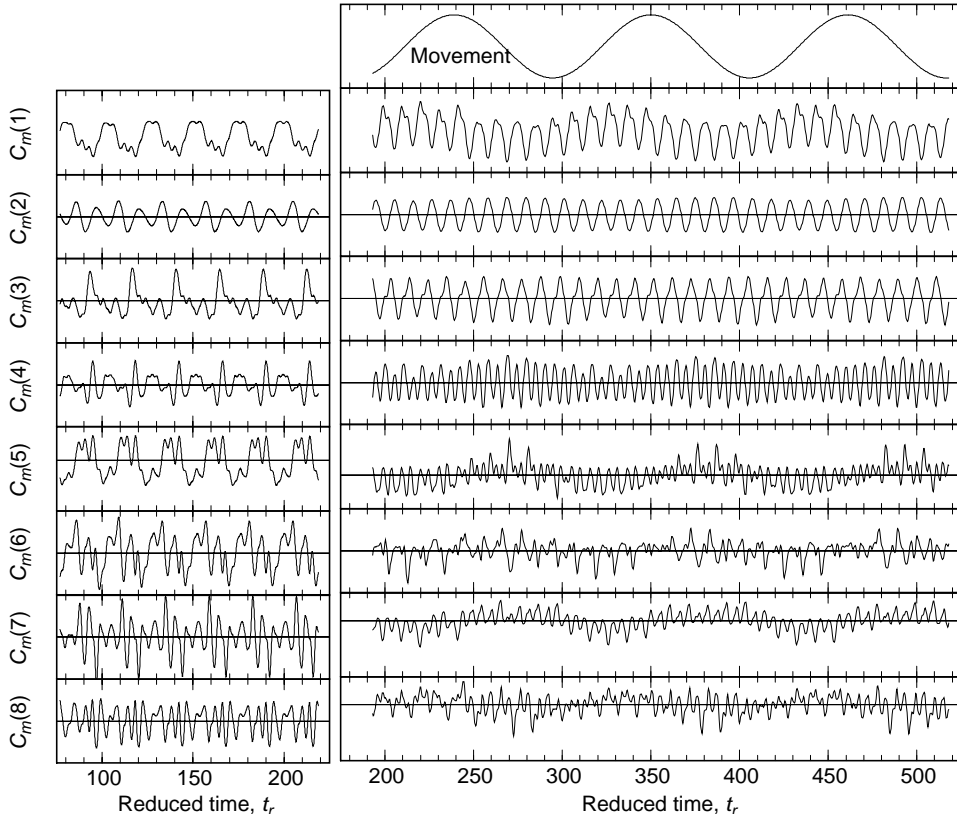


Figure 25. Time histories of the pitching moment decomposition in static and galloping ($V_r = 110$) cases.

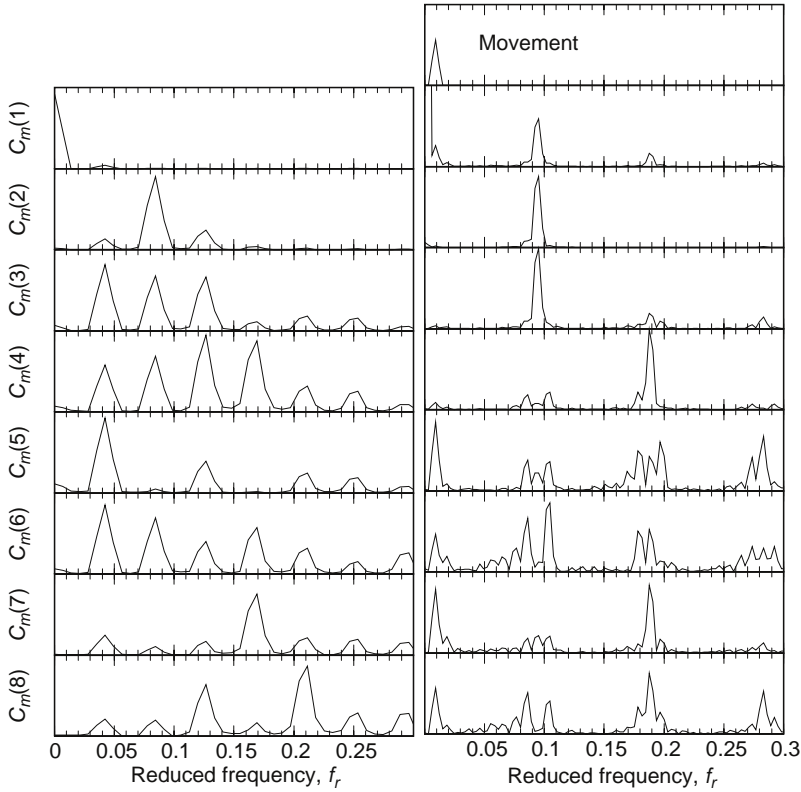


Figure 26. Fourier Transforms of the pitching moment decomposition in static and galloping ($V_r = 110$) cases.

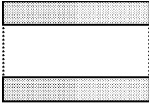
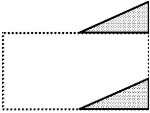
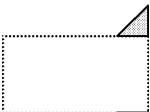
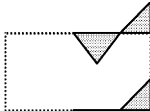
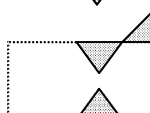
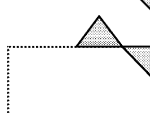
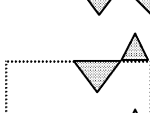
reattachments on the lateral sides (impinging secondary vortices) and their interactions with the alternate leading-edge vortex shedding induce large perturbations on the pitching moment. The frequencies of these perturbations are $\frac{1}{2}St$ and its harmonics. The most energetic phenomenon for the fluctuations of the drag in the static case is located on this subharmonic frequency.

It is interesting to note that, for galloping, the present configuration leads to the alternate vortex shedding as being globally the most energetic phenomenon (i.e., the larger eigenvalues), and not the forced oscillation component. Also, for pitching oscillations (Amandolèse 2001), the same behaviour was found for an aspect ratio of 4, while the larger ratios were characterised by the forced movement as being the most energetic mechanism.

The analysis of the shapes for the lateral sides is presented in detail in Table 7. In each case, a simplified shape is reproduced and interpreted. The main frequency of its time history is noted for the two cases, static and galloping, and the link is made with the relative magnitude of the force (i.e., the lift and the pitch for the lateral sides). When many harmonics appear, the index n is placed besides the frequency concerned, so that the term $n St$ means that the Strouhal number and its multiples appear.

It must be noted that the impinging, made prominent by the POD, occurs mainly at two positions along the chord of the cylinder, at e (or $c/2$) starting from the leading edge, or at $3e/2$. In the first case, the phenomenon involved is linked to the leading-edge vortices, at frequency St , and in the second case to secondary vortices at frequency $\frac{1}{2}St$ and possibly its harmonics.

TABLE 7
Analysis of the lateral side mode shapes from the POD

Lateral side shape	Physical interpretation	Static case	($V_r=0$)	MIV case	($V_r=110$)
	Mean pressure value	0	Mode 1	0	Mode 1
	Antisymmetric stall Leading-edge vortex Shedding	St	Lift 1 Mode 2	St	Lift 1 Mode 2
	Antisymmetric Impinging at e	$n \text{ St}/2$	Pitch 3 ~ Mode 3	St	Pitch 1 Mode 3
	Antisymmetric Impinging at $3/2 e$	$n \text{ St}/2$	Pitch 1 Mode 4	$f_r + n \text{ St}$	Pitch 2 Mode 5
	Symmetric Impinging at $3/2 e$	$n \text{ St}/2$	Pitch 5 Mode 6	2 St	Pitch 7 Mode 4
	Antisymmetric Impinging at e			$f_r + n \text{ St}$	Pitch 5 Mode 5
	Symmetric Impinging at e			$f_r + 2 \text{ St}$	Mode 7
	Antisymmetric Impinging at $3/2 e$	$\frac{3}{2} \text{ St}$ $\frac{5}{2} \text{ St}$	Pitch 8 Mode 8		
	Antisymmetric Impinging at e	2 St	Pitch 6 Mode 7		
	Symmetric Impinging at e			$f_r + n \text{ St}$	Pitch 4 Mode 6

In the galloping regime, for the lateral sides, the movement at f_r appears only for higher order functions, not below mode 5. Another point is that the subharmonic $\frac{1}{2}St$ and its multiples are not present because of the symmetry of the secondary vortices induced by the movement, as already noted.

4.2. GALLOPING FORCE MODEL

The objective of this part of the paper is to provide a simplified model of the galloping phenomenon that could be applied to practical situations, starting from static measurements on the section concerned. It is well known that quasi-steady theory does not produce reliable results for the critical velocity, because the aerodynamic damping expressed in the Den Hartog criterion does not take into account the dynamic part of the stalled flow.

We start from the equation of motion of a 2-D cylinder vibrating in the z direction

$$m \ddot{z}(t) + 2\eta\omega m \dot{z}(t) + m\omega^2 z(t) = F_z(\dot{z}(t - \tau)), \tag{18}$$

where F_z is the aerodynamic force along the z -axis, which depends on the velocity of the cylinder with a little time lag τ , as initially proposed by Hémon (1999a). In the quasi-steady theory (QST), this time lag or phase lag is neglected. The aerodynamic force is written in a classical way as

$$F_z(\dot{z}(t - \tau)) = \frac{1}{2}\rho c V_a^2 C_z(\alpha_a), \tag{19}$$

where the relative velocity V_a and the relative angle of attack α_a are due to the movement of the cylinder, and they are obtained by a velocity triangle which gives

$$V_a^2 = V^2 + \dot{z}^2(t - \tau) - 2V \sin \alpha \dot{z}(t - \tau), \quad \tan(\alpha_a) = \frac{V \sin \alpha - \dot{z}(t - \tau)}{V \cos \alpha}. \tag{20}$$

The static coefficient C_z is a function of the angle of attack and can be expressed in terms of C_D and C_L . Then, a linear analysis, combined with an energy balance starting from equation (18) allows finding the critical velocity of the flow above which the cylinder will start its galloping oscillations. We assume that the movement takes the harmonic form

$$z(t) = Z_M \sin \omega t, \tag{21}$$

and we can then find the critical velocity using the dimensionless numbers, i.e., the reduced velocity V_r , the Scruton number Sc and the reduced time lag τ_r . Hence, one obtains

$$\frac{V_{rc}}{4\pi Sc} + \frac{c}{eA_z \cos(2\pi\tau_r/V_{rc})} = 0 \tag{22}$$

which can be easily solved numerically, knowing $A_z = 2C_z \sin \alpha + (\partial C_z / \partial \alpha) \cos \alpha$ from static measurements.

The interesting point comes from the time lag that has to be estimated accurately because it plays a fundamental role in the energy exchanges between the flow and the structure. As pointed out recently (Deniz & Staubli 1998), unsteady airfoil theory (UAT) (Fung 1955) already takes into account a time lag, since the lift force is expressed using the complex function of Theodorsen $F(k) + iG(k)$, which depends on the angular reduced frequency k :

$$F_z = -\chi\rho\pi\left(\frac{c}{2}\right)^2 \ddot{z} - \rho V\left(\frac{c}{2}\right) C'_z F(k)\dot{z} + \rho V^2\left(\frac{c}{2}\right) C'_z kG(k)z, \tag{23}$$

where χ is an added mass coefficient which is generally neglected for such a low speed air-flow. Thus the time lag is given by

$$\tau_r = \frac{1}{k} \arctan\left(\frac{-2F(k)}{G(k)}\right) \quad (24)$$

when the added mass is neglected. However, this theory assumes that the flow is not stalled and is non viscous, and therefore the time lag estimated by equation (24) gives very small values for the range of reduced velocities of our study. The UAT results are close to those obtained with the quasi-steady assumption, and therefore an improvement has to be found. Indeed, the time lag is a consequence of the viscosity and becomes very large when the flow is stalled, because it simply translates the fact that the flow is not restored instantaneously when the structure moves.

For bluff bodies in general, the time lag remains an unknown parameter, but some information exists for the case of interference galloping between two cylinders in tandem, where the phase lag triggers the instability. Indeed, some authors such as Blevins (1990) and the results found in Hémon (1999b) showed a correlation between the reduced time lag and the Strouhal number, i.e., the period of the vortex shedding. From another point of view, some links exist between the time lag and the convection velocity near the body and the width of the wake. Therefore, the time lag was chosen as one period of the vortex shedding, so that by definition the reduced time lag is taken equal to the inverse of the Strouhal number. The explanation for such a correlation remains unclear, but some good results are obtained by comparison with experiments, as shown below. A thorough understanding requires further investigation.

The results of calculations are given in Tables 8 and 9 for the rectangular and square sections, respectively, in smooth flow. The static lift coefficients were taken from Deniz & Staubli (1997) for the rectangular section in smooth flow and from Luo *et al.* (1994) for the square cylinder. The computations were performed with smoothing polynomials for the force coefficients. The reduced velocities presented are divided by $4\pi Sc$, which produces a

TABLE 8
Critical velocities for the rectangular section in smooth flow

$c/e=2$	$\alpha=0^\circ$	$\alpha=2^\circ$	$\alpha=4^\circ$	$\alpha=6^\circ$
C'_z	-4.86	-4.51	-3.05	+0.34
St	0.085	0.087	0.120	0.141
$V_{rel}/4\pi Sc$ experiments	0.23	0.23	0.23	Stable
$V_{rel}/4\pi Sc$ equation (22)	0.233	0.238	0.235	Stable
UAT or QST	0.10	0.11	0.16	Stable

TABLE 9
Critical velocities for the square section in smooth flow

$c/e=1$	$\alpha=0^\circ$	$\alpha=10^\circ$
C'_z	-2.05	-8.16
St	0.127	0.134
$V_{rel}/4\pi Sc$ experiments	>0.28	0.15
$V_{rel}/4\pi Sc$ equation (22)	0.32	0.16
UAT or QST	0.24	0.06

TABLE 10
Critical velocities for the rectangular section in turbulent flow at 5% intensity

$c/e=2$	$\alpha=0^\circ$	$\alpha=2^\circ$	$\alpha=4^\circ$
C'_z	-2.43	-0.89	+1.51
St	0.037	0.043	None
$V_{rc}/4\pi$ Sc experiments	0.15	0.19	Stable
UAT or QST	0.20	0.56	Stable

kind of universal reduced velocity, as suggested by Novak (1972). Indeed, his experimental results for the rectangular section at $\alpha=0$ are in agreement with the present results. For the square section at $\alpha=0$, the critical velocity could not be reached experimentally and the maximum value explored was 0.28. Indeed, the model gives 0.32, whereas the QST gives 0.24 which should have been observed experimentally. Thus, the proposed time-delayed calculation of the critical velocity is in very good agreement with the experiments in smooth flow and improves significantly the quasi-steady theory, assuming that the Strouhal number of the section is known.

However, when vortex shedding does not occur, or when it is not well established, the model cannot give reliable results. Table 10 presents the results for the rectangular section with 5% turbulence intensity. The static lift coefficient used is the one given in Fig. 3. The QST calculation does not give good results and predicts much higher critical velocities, whereas the experiments give the opposite. The proposed model with time delay based on the period of vortex shedding also does not give good results, because the Strouhal number under such turbulent conditions is not the same as in smooth flow. Moreover, the Strouhal number is very difficult to measure, because the signal is very noisy and the vortex shedding not well established, as was already mentioned.

Anyhow, if formula (22) is used with the critical velocity given by the experiments, it is impossible to find an equivalent reduced time lag which could make the model work. Indeed, in this case the ratio between the time lag and the period of the movement

$$\tau/T = f_r/\text{St} \quad (25)$$

gives 0.64 in turbulent flow, whereas the same ratio is only 0.18 in smooth flow. Thus, according to the proposed model, when the force is delayed too long in comparison with the period of the movement, there is no possibility for the fluid to transfer energy to the structure, which is not in agreement with the experiments. Therefore, galloping oscillations at such low reduced velocities must be subject to another physical mechanism which is not reproduced in the present model or in QST or UAT. The interaction with vortex shedding, even if it is perturbed here by the free-stream turbulence, is probably responsible for this, as was shown for the square section by Bearman *et al.* (1987).

5. CONCLUSIONS

An experimental and numerical study of the aeroelastic behaviour of slender rectangular- and square-section cylinders was presented.

The experiments were performed with a flexible cylinder clamped at both ends, which led to unusual lock-in of the vortex shedding with different bending modes, although the final steady oscillations occurred in the fundamental mode. The low Reynolds number of the study might be an important parameter.

In the galloping regime, critical velocities were detected which do not correspond to calculations using the quasi-steady theory. In particular, a small increase in the free-stream turbulence intensity reduces the critical velocity, a fact which, as far as we know, has not been reported before. A simple model of galloping was proposed to fit the experiments better, but some of the configurations in turbulent flow are probably interacting with the vortex shedding, making the model ineffective. This model is based on a time-delayed force, where the time lag is linked to the main period of natural vortex shedding. As long as the Strouhal number exists and is larger than the reduced frequency, the proposed model can be used, and it improves the standard quasi-steady theory.

Wall-pressure distributions, obtained numerically on a 2-D rectangular section, were analysed using the proper orthogonal decomposition technique. New indicators were proposed in order to link the proper functions with the aerodynamic force components, and then the proper shapes of the pressure were classified. It was shown, by comparing the static and forced oscillation cases in the galloping range, that secondary vortices inside the shear layer become symmetrical and their effect on the forces is cancelled. Moreover, it was found that not all the proper shapes are involved in the aeroelastic coupling, some of them being similar with and without vibrations.

These conclusions might not be correct for higher aspect ratios, such as those of a bridge deck, where coupling with the movement is of a different kind. In any case, the POD technique showed a great potential for analysing pressure data, especially for the aeroelastic problem, and its application should become generalised for experimental data processing.

REFERENCES

- AMANDOLESE, X. 2001 Contribution à l'étude des chargements fluides sur des obstacles non profilés fixes ou mobiles. Ph. D. Thesis, Ecole Nationale des Ponts & Chaussées, Paris, France.
- BEARMAN, P. W. & OBASAJU, E. D. 1982 An experimental study of pressure fluctuations on fixed and oscillating square-section cylinders. *Journal of Fluid Mechanics* **119**, 297–321.
- BEARMAN, P. W., GARTSHORE, I. S., MAULL, D. J. & PARKINSON, G. V. 1987 Experiments on flow-induced vibration of a square-section cylinder. *Journal of Fluids and Structures* **1**, 19–34.
- BLEVINS, R. D. 1990 *Flow-Induced Vibrations*, pp. 104–110. New York: Van Nostrand Reinhold.
- DAVIS, R. W. & MOORE, E. F. 1982 A numerical study of vortex shedding from rectangles. *Journal of Fluid Mechanics* **116**, 475–506.
- DEN HARTOG, J. P. 1934. *Mechanical Vibrations*, pp. 299–305. New York: Dover edition (1985).
- DENIZ, S. & STAUBLI, T. 1997 Oscillating rectangular and octogonal profiles: interaction of leading and trailing edge vortex formation. *Journal of Fluids and Structures* **11**, 3–31.
- DENIZ, S. & STAUBLI, T. 1998 Oscillating rectangular and octogonal profiles: modelling of fluid forces. *Journal of Fluids and Structures* **12**, 859–882.
- DOWELL, E. H., HALL, C., THOMAS, J. P., FLOREA, R., EPUREANU, B. I. & HEEG, J. 1998 Reduced order models in unsteady aerodynamics. Proceedings of the 3rd *International Conference on Aero-Hydroelasticity*, Prague, August 30–September 3, pp. 20–35.
- FARGE, M. 1992 Wavelet transforms and their applications to turbulence. *Annual Review Fluid Mechanics* **24**, 395–457.
- FUNG, Y. C. 1955 *An Introduction to the Theory of Aeroelasticity* pp. 395–407. New York: Dover edition (1993).
- GARTSHORE, I. S. 1973 The effects of free-stream turbulence on the drag of rectangular two-dimensional prisms. BLWTL Report 4-73. University of Western Ontario, London, Ont. Canada.
- GERADIN, M. & RIXEN, D. 1993 *Théorie des vibrations—Application à la dynamique des structures*, pp. 74–76. Paris: Masson.
- GIRAULT, V. & RAVIART, P. A. 1986 *Finite Element Methods for Navier–Stokes Equations*. Berlin: Springer-Verlag.

- HAAN, F. L. Jr., KAREEM, A. & SZEWCZYK, A. A. 1998 The effects of turbulence on the pressure distribution around a rectangular prism. *Journal of Wind Engineering and Industrial Aerodynamics* **77/78**, 381–392.
- HÉMON, P. 1999a Approach of galloping vibrations using a time-delayed force modelling and experimental validation. *Compte Rendu de l'Académie des Sciences de Paris, Série II b*, 327, 679–684.
- HÉMON, P. 1999b An Improvement of the time delayed quasi-steady model for the oscillations of circular cylinders in cross-flow. *Journal of Fluids and Structures* **13**, 291–307.
- HÉMON, P. & SANTI, F. 2000 Vortex-induced vibrations of an elongated rectangular beam. In *Flow-Induced Vibration*, (eds. S. Ziada & T. Staubli) Lucerne 19–22 June 2000, Balkema, pp. 123–130.
- HÉMON, P., SANTI, F., SCHNOERRINGER, B. & WOJCIECHOWSKI, J. 2001 Influence of the free-stream turbulence on the movement-induced vibrations of an elongated rectangular cylinder in cross-flow. *Journal of Wind Engineering and Industrial Aerodynamics* **89**, 1383–1395.
- HINZE, J. O. 1975 *Turbulence*, 2nd edition. New York: McGraw-Hill.
- HOLMES, P., LUMLEY, J. L. & BERKOOZ, G. 1996 *Turbulence, Coherent Structures and Symmetry*. Cambridge: Cambridge University Press.
- JEONG, S. H., BIENKIEWICZ, B. & HAM, H. J. 2000 Proper orthogonal decomposition of building wind pressure specified at non-uniformly distributed pressure taps. *Journal of Wind Engineering and Industrial Aerodynamics* **87**, 1–14.
- LEBART, L., MORINEAU, A. & FENELON, J.-P. 1982. *Traitement des données statistiques* 2ème édition, pp. 283–295. Paris: Dunod.
- LETCHFORD, C. W. & SARKAR, P. P. 2000 Mean and fluctuating wind loads on rough and smooth parabolic domes. *Journal of Wind Engineering and Industrial Aerodynamics* **88**, 101–117.
- LI, Q. S. & MELBOURNE, W. H. 1995 An experimental investigation of the effects of free-stream turbulence on streamwise surface pressures in separated and reattaching flow. *Journal of Wind Engineering and Industrial Aerodynamics* **54/55**, 313–323.
- LUO, S. C., YAZDANI, M. D. G., CHEW, Y. T. & LEE, T. S. 1994 Effects of incidence and afterbody shape on flow past bluff cylinders. *Journal of Wind Engineering and Industrial Aerodynamics* **53**, 375–399.
- MATSUMOTO, M., ISHIZAKI, H., MATSUOKA, C., DAITO, Y., ISHIKAWA, Y. & SHIMAHARA, A. 1998 Aerodynamic effects of the angle of attack on a rectangular prism. *Journal of Wind Engineering and Industrial Aerodynamics* **77/78**, 531–542.
- MATSUMOTO, M. 2000 Aeroelasticity and bridge aerodynamics. International Advanced School on Wind-Excited and Aeroelastic Vibrations of Structures. Genova, June 12–16.
- NAKAMURA, Y. & OHYA, Y. 1983 The effects of turbulence on the mean flow past square rods. *Journal of Fluid Mechanics* **137**, 331–345.
- NAKAMURA, Y. & OHYA, Y. 1984 The effects of turbulence on the mean flow past two-dimensional rectangular cylinders. *Journal of Fluid Mechanics* **149**, 255–273.
- NAKAMURA, Y. & NAKASHIMA, M. 1986 Vortex excitation of prisms with elongated rectangular, H and T cross-sections. *Journal of Fluid Mechanics* **163**, 149–169.
- NAUDASCHER, E. & ROCKWELL, D. 1994 *Flow-Induced Vibrations: An Engineering Guide*, pp. 200–208 and 308–320. Rotterdam: Balkema.
- NOVAK, M. 1969 Aeroelastic galloping of prismatic bodies. *ASCE Journal of the Engineering Mechanics Division* **95**, 115–142.
- NOVAK, M. 1972 Galloping oscillations of prismatic structures. *ASCE Journal of the Engineering Mechanics Division* **98**, 27–46.
- NOVAK, M. & TANAKA, H. 1974 Effect of turbulence on galloping instability. *ASCE Journal of the Engineering Mechanics Division* **100**, 27–47.
- NORBERG, C. 1993 Flow around rectangular cylinder: pressure forces and wake frequencies. *Journal of Wind Engineering and Industrial Aerodynamics*, **49**, 187–196.
- OBASAJU, E. D., ERMHAUS, R. & NAUDASCHER, E. 1990 Vortex-induced streamwise oscillations of a square-section cylinder in a uniform stream. *Journal of Fluid Mechanics* **213**, 171–189.
- OKAJIMA, A. 1988 Numerical simulation of flow around rectangular cylinders. *Proceedings of Bluff Body Aerodynamics & Applications*, BBAA, (eds. M. Ito, M. Matsumoto & N. Shiraishi), Kyoto, Japan.
- ONGOREN, A. & ROCKWELL, D. 1988 Flow structure from an oscillating cylinder. Part 1. Mechanisms of phase shift and recovery in the near wake. *Journal of Fluid Mechanics* **191**, 197–223.
- PIRONNEAU, O. 1989 *Finite Element Methods for Fluids*. Paris: Masson.
- SAATHOFF, P. & MELBOURNE, W. H. 1999 Effects of freestream turbulence on streamwise pressure measured on a square-section cylinder. *Journal of Wind Engineering and Industrial Aerodynamics* **79**, 61–78.

- SIMIU, E. & SCANLAN, R. H. 1986. *Wind Effects on Structures*, 2nd edition. New York: Wiley.
- TAMURA, T., ITOH, Y., WADA, A. & KUWAHARA, K. 1993: Numerical investigation on the aeroelastic instability of bluff cylinders. *Journal of Wind Engineering and Industrial Aerodynamics*, **46-47**, 557–566.
- TAMURA, Y., SUGANUMA, S., KIKUCHI, H. & HIBI, K. 1999 Proper orthogonal decomposition of random wind pressure field. *Journal of Fluids and Structures* **13**, 1069–1095.
- VAN OUDHEUSDEN, B. W. 2000 Aerodynamic stiffness and damping effects in the rotational galloping of a rectangular cross-section. *Journal of Fluids and Structures* **14**, 1119–1144.

APPENDIX: NOMENCLATURE

α	angle of attack, degree
δ_{nm}	Kronecker symbol, 1 if $n = m$, 0 otherwise
η	damping ratio
η_1	Nonlinear damping coefficient
λ_i	i th eigenvalue
μ_i	i th principal component in the POD
ν	air viscosity, m^2/s
ρ	air density, kg/m^3
τ	time lag, s
τ_r	reduced time lag, $\tau_r = \tau V/e$
ω	circular frequency, rad/s
c	chord (flowwise dimension) of the cylinder, m
C_M	pitching moment coefficient referred to the centre of mass
C_x	drag coefficient
C_z	lift coefficient
e	thickness of the cylinder, m
f	bending frequency, Hz
f_r	reduced frequency $f_r = fe/V$
f_v	frequency of vortex shedding, Hz
I	turbulence intensity (longitudinal component)
k	angular reduced frequency, $k = 2\pi f_r$
L	length (spanwise) of the cylinder, m
L_x	longitudinal length scale of turbulence, m
m	mass of the cylinder per unit length, kg/m
M	mesh size of the turbulence generation grid, m
$P(\mathbf{X}, t)$	wall pressure distribution, function of space \mathbf{X} and time t
Re	Reynolds number, $\text{Re} = Vc/\nu$
\mathbf{R}_c	correlation matrix of the pressure distribution
Sc	Scruton number, $Sc = 2\eta m/\rho e^2$
St	Strouhal number $St = f_v e/V$
t_r	reduced time $t_r = tV/e$
V	wind mean velocity, m/s
V_r	reduced velocity, $V_r = 1/f_r$
\mathbf{W}_i	i th eigenvector or proper function
x	longitudinal coordinate
z	vertical coordinate
\dot{z}	vibration velocity of the cylinder (vertical), m/s